文章编号：1001-9014(2022)06-1042-09

DOI:10.11972/j.issn.1001-9014.2022.06.014

Theoretical study and PIC simulation of a 220 GHz Gyro-TWT with periodic dielectric loaded waveguide

CHEN Ru-Tai, YU Sheng

(School of Electronic Science and Engineering, University of Electronic Science and Technology of China, Chengdu 611731, China)

Abstract: In this article, a 220 GHz gyro-TWT operating at fundamental harmonic TE01 mode with periodic dielectric loaded (PDL) waveguide was designed through theoretical study and particle in cell (PIC) simulation. The parasitic oscillations (absolute instability oscillation and backward wave oscillation) have been successfully suppressed by study of start-up thresholds and loading dielectric rings. The beam wave interaction behaviors are compared between nonlinear theory programs and PIC simulation, the results are basically consistent. In PIC simulation, the optimized gyro-TWT was developed with saturated output power of 55.61 kW, corresponding efficiency of 26.48% at 220 GHz with 70 kV and 3A electron beam, the saturated gain is 53.56 dB, and -3dB bandwidth is 12 GHz.

Key words: gyrotron traveling wave tube (Gyro-TWT), parasitic oscillations, periodic dielectric loaded, nonlinear theory, particle in cell (PIC), 220 GHz.

220 GHz周期介质加载波导回旋行波管的理论设计与PIC仿真

陈儒泰, 喻 胜

(电子科技大学 电子科学与工程学院,四川 成都 611731)

摘要:通过理论研究和粒子仿真(Particle in Cell , PIC),设计了一支工作在基波TE01模式下,采用周期性介质加载(PDL)波导的220 GHz回旋行波管(gyrotron traveling wave tube, Gyro-TWT)。通过研究寄生振荡的起振阈值和加载介质环,成功抑制了寄生振荡(绝对不稳定性振荡和返波振荡)。分别采用了非线性理论程序与粒子仿真对注波互作用进行研究,对比了两种结果基本一致。PIC仿真结果显示,优化后的回旋行波管,工作在220 GHz时,在输入70 kV和3 A电子注的情况下,饱和输出功率为55.61 kW,对应的效率为26.48%,饱和增益为53.56 dB,-3 dB带宽为12 GHz。

关 键 词:回旋行波管;寄生振荡;周期介质加载;非线性理论;粒子模拟;220 GHz

中图分类号:O43 **文献标识码**:A

Introduction

Gyrotron traveling wave tube (Gyro-TWT) is a kind of relativistic nonlinear vacuum electric device that can generate high power, high gain and wideband in microwave, millimeter wave and terahertz wave band. It has broad application prospects in high resolution radar, high speed communication, electric countermeasure etc., and attracted the attention of many research institutions [1-2]. High frequency interaction structure is one of the core components in Gyro-TWT, where is the mainly place that process the beam-wave interaction and possible to occur the parasitic oscillations (absolute instability oscillation and backward wave oscillation). In early stage, the interaction structure usually is smooth waveguide, where the parasitic oscillations are easily to happen and seriously affect the performance of Gyro-TWT[2-3]. For suppressing of parasitic oscillations, the interaction structure has evolved into many improved structures. In 1990s, the National Tsinghua University (NTHU) has developed an ultrahigh gain ka-band Gyro-TWT with distributed loss loading circuit, the saturated peak power is 93 kW with 26.6% efficiency, 70 dB gain

Received date: 2022-06-13, **revised date**: 2022-08-29 **收稿日期**:2022-06-13,**修回日期**:2022-08-29

Biography: Chen Ru-tai (1995-), male, Yanggu China, Ph. D. Research area involves high-frequency and high-power millimeter and terahertz wave device. E-mail: rutaichen@outlook.com

and -3 dB bandwidth of 3 GHz [4]. As this report published, the Gyro-TWT has entered the rapid development era. In 2014, the University of electronic science and technology of China (UESTC) has tested a W-band with a nonuniform periodic dielectric loaded waveguide gyro-TWT, the peak output power is 112kW with efficiency of 23.3% at 93.5 GHz, and the bandwidth of greater than 90kW is about 4 GHz [5]. In the process of developing towards higher frequency band, in 2003, the Massachusetts Institute of Technology (MIT) has reported a 140 GHz confocal Gyro-TWT, with the mode selective circuit, the pulsed power is up to 30kW with an efficiency of 12%, a gain of 29 dB and bandwidth of 2.3 GHz [6]. In 2017, MIT also has reported a 250 GHz photonic-band-gap gyro-TWT with picosecond pulses, a circuit gain of more than 55 dB and a wide operational bandwidth of 16 GHz are observed [7]. Besides, a 220 GHz confocal gyro-TWT with two lossy severs is designed in UESTC, peak output power reaches 10.7kW with a efficiency of 11.65%, a peak gain of 25.5 dB and 1 dB bandwidth of 2.3 GHz [8]. In 2019, the National University of Defense Technology has reported a 220 GHz second harmonic confocal gyro-TWT with an output power of 4.55 W, the efficiency of 2.2%, gain of 21.8 dB and the -3 dB bandwidth of 6 GHz [9]. Of course, PDL interaction structure still is the most matured and effective interaction circuit, which has been chosen to design the 220 GHz gyro-TWT [10-12].

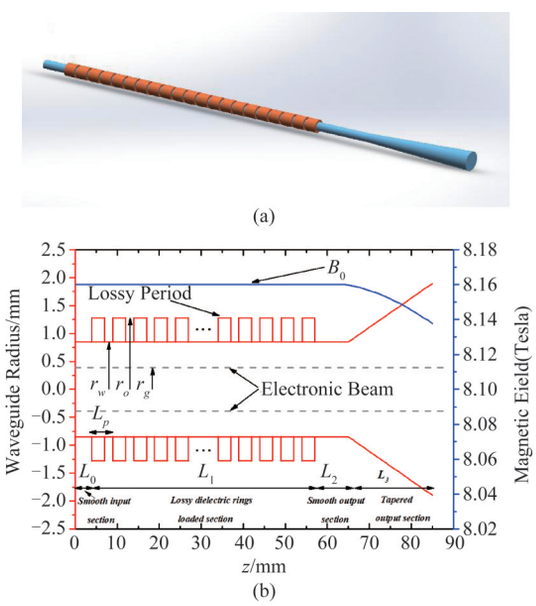

Fig. 1 Beam-wave interaction circuit configurations of the 220 GHz Gyro-TWT (a) The 3-D structure diagram, (b) the interaction circuit schematic

图1 220 GHz回旋行波管注波互作用示意图 (a) 3维结构,(b) 电路详解图

In this article, a fundamental harmonic TE_{01} mode 220 GHz gyro-TWT is designed through theoretical study and PIC simulation. For suppressing of potential parasitic oscillations, the start-up thresholds are analyzed in detail and compared with PIC simulation results. By the theoretical analyses, the interaction circuit preliminary operating parameters were obtained. To get more accurate results, the designed Gyro-TWT also was simulated in 3D-PIC (CST) simulation software. The organization of this article as follows: Section II, the parasitic oscillations of interaction circuit are introduced, linear and nonlinear theory are used to obtain the initial operating parameters. Section III, the PIC simulation results of the present PDL gyro-TWT are described and compared with theoretical studies.

1 Beam-wave interaction theoretical study

The 220 GHz Gyro-TWT beam-wave interaction circuit schematic is shown in Fig. 1. As a periodic dielectric loaded (PDL) interaction circuit is usually combined with four parts, smooth input section, lossy dielectric rings loaded section, smooth output section and tapered output section, respectively. The detailed theoretical analyses, and design of the interaction structure are discussed in this section.

1.1 Potential parasitic oscillation

As the main factor limiting the development of Gyro-TWT, the parasitic oscillations of interaction circuit prime are absolute instability oscillation and backward wave oscillation (BWO). As the electron beam of Gyro-TWT is working on the weakly relativistic situation, and for getting high gain, the working area always is chosen near the grazing point, as the red circular area in Fig. 2, named convective instability area. But when the working current increase to a certain value (oscillation start-up current), the working area will extend to the negative area of wave number. And then, the absolute instability oscillation has occurred. For backward wave oscillation, when the electron cyclotron resonance curve intersects the waveguide mode dispersion curve in the negative wave number area. In this area, the phase and group velocity of the electromagnetic wave are negative, the angular frequency of electron and wave are quite closed. When the backward wave and the forward moving electron meet together, and if the current or interaction waveguide length bigger than the start oscillation threshold, the operating conditions will satisfy the needs of backward wave oscillation, there will generate the energy feedback loop in the interaction structure, and the backward wave oscillation is formed. In Fig. 2, when the mode TE_{01} as the operating mode, two electron cyclotron resonance curves ($s=1$, $s=2$) have intersected with mode (TE_{11}, TE_{21}, TE_{02}) dispersion curve in the negative wave number area (Point A, B, C in Fig. 2), where maybe occur the BWO.

For the suppressing of BWO and absolutely instability oscillation, reducing of operating current and pitch ratio, increasing of magnetic detuning ratio both are effective. And the detailed analyses will be presented in the below.

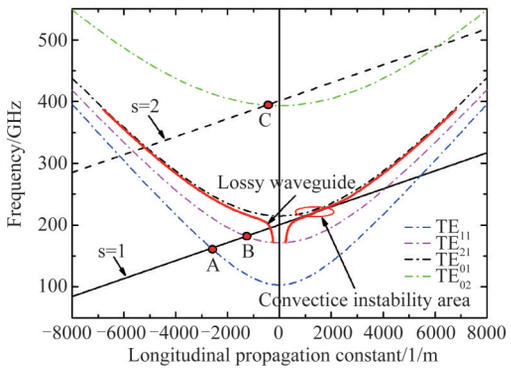

Fig. 2 Dispersion diagram of 220 GHz PDL Gyro-TWT, (U_0 = 70 kV, beam velocity pitch factor α = 1.2, magnetic detuning ratio b = 0.98. Point A, B, C are backward wave oscillation points. The red circular area is convective instability area)

图2 220 GHz周期介质加载回旋行波管色散曲线(电子注电压为U_0 = 70 kV,电子注横纵速度比α = 1.2,磁场失谐率b = 0.98。点A,B,C为返波振荡起振点。红色圆圈为绝对不稳定性区域)

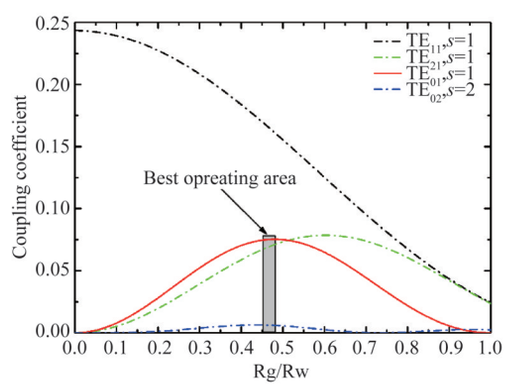

Fig. 3 The coupling coefficient of 220 GHz PDL Gyro-TWT versus normalized guide center radius

图3 220 GHz周期介质加载回旋行波管耦合系数与归一化引导中心半径的关系

1.2 Linear theory analysis

In general, Gyro-TWT operates at fundamental mode, which can lead the device to operate in low mode density conditions, and directly reduce the occurrence of parasitic oscillations. Meantime, as the operating frequency increases, the size of the interaction waveguide decreases accordingly. So, in this paper, the operating mode of 220 GHz Gyro-TWT is set as TE_{01}, and the waveguide radius r_w is 0.85 mm. Besides, a high alpha value can improve the efficiency, but also is a serious challenge for the design of the MIG, which usually comes with larger velocity spread problems. So, the electron beam velocity ratio (alpha) is set to be 1.2 in our design.

Based on the linearized Vlasov-Maxwell equation and the plasma kinetic model, the linear theory has been derived. And taking the lossy loading into consideration. The small- signal dispersion equation of dielectric-loaded

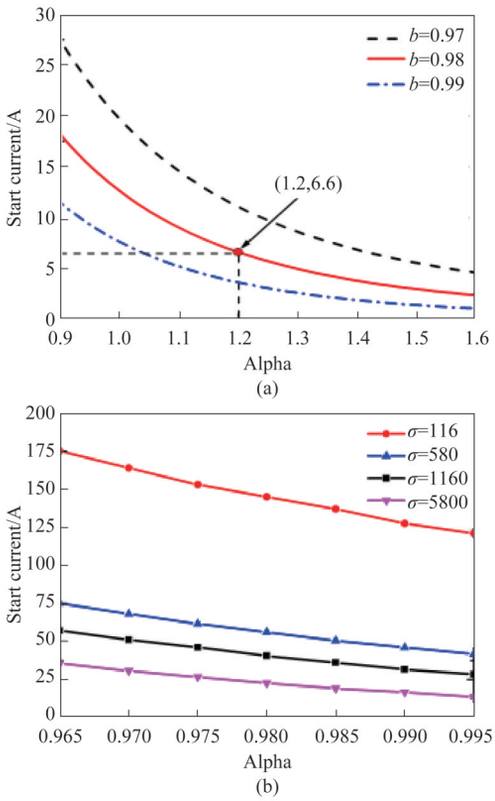

Fig. 4 The start current of absolute instability oscillation U_0 = 70 kV, (a) losses circuit with different b, (b) lossy circuit with different conductance

图4 绝对不稳定性振荡起振电流,电压U_0 = 70 kV (a) 无损波导情况下不同磁场失谐率的起振电流曲线,(b)损耗加载波导情况下不同电导率下的起振电流曲线

cylindrical waveguide Gyro-TWT can be written as [3-4]:

$$D(\omega,k_z)=\frac{\omega^2}{c^2}-k_z^2-k_{mn}^2\left[1-(1+i)\left(1+\frac{m^2}{\mu_{mn}^2-m^2}\right)\frac{\delta}{r_w}\frac{\omega^2}{\omega_c^2}\right]+\frac{4I}{r_w^2 I_A K_{mn}}\left[\frac{\beta_\perp^2(\omega^2-c^2k_z^2)H_{lm}(k_{mn}r_c,k_{mn}r_L)}{(\omega-k_z v_z-l\Omega_c/\gamma)^2}\right]=0 \quad , \quad (1)$$

where ω is the wave angular frequency, c is the light speed in the vacuum, $k_z=\sqrt{(\omega/c)^2-k_{mn}^2}$ is the axial propagation wave number, $k_{mn}=\mu_{mn}/r_w$ is the cutting off wave number, μ_{mn} is the nth root of mth Bessel function, $I_A\approx 17\beta_z\gamma(\mathrm{kA})$ is the Alfven current, r_w, r_L, r_c, v_z, $\beta_\perp$, δ, l and Ω_c represent the waveguide radius, the electron Lamer radius, the electron beam guiding radius, the electron axial velocity, the electron orbital velocity normalized to c, the skin depth of loaded waveguide, the cyclotron harmonic number, and the non-relativistic electron cyclotron frequency, respectively. And the other parameters are defined as:

$$K_{mn}=J_m^2(\mu_{mn})(1-m^2/\mu_{mn}^2) \quad , \quad (2)$$

$$H_{lm}(k_{mn}r_c,k_{mn}r_L)=J_{l-m}^2(k_{mn}r_c)J_l'^2(k_{mn}r_L) \quad , \quad (3)$$

The Eq. 3, H_{lm} can be used to describe the electron beam and wave mode coupling coefficient. Figure 3 is the relationship between the coupling coefficient factor and normalized guiding radius. We can see that the TE_{11} mode coupling factor always maintain the advantage over the whole radius area. It means that the backward wave oscillation of TE_{11} mode is quite likely to occur, which needs to be suppressed more carefully. And when $r_c = 0.48r_w$ the operating mode gets the biggest coupling factor, but TE_{21} mode factor also is very closed. In order to avoid the potential parasitic oscillation. A guiding center radius of $r_c = 0.46r_w$ was selected.

Figure 4(a) shows the changing of absolute oscillation start current with α, in a losses circuit. When $\alpha = 1.2$ and $b = 0.98$ the start current is 6.6 A. For the stable operation of the device, away from the start current threshold, 3 A is chosen as the operating current. Figure 4 (b) is the start current of absolute oscillation of lossy circuit, it's clearly, when b increases, the start current decreases gradually. And, with the dielectric conductance σ decreasing, the start current also increases significantly.

In addition to the absolute oscillation, the backward wave oscillation is another kind of parasitic oscillation which is also seriously impacts the device's performance. For analysis of this kind of oscillation, applying the Laplace transformation to solve the Valsov-Maxwell equation [3-4], the longitudinal field amplitude can be acquired. Figure 5 (a) shows the start length of three potential backward wave oscillations with their related oscillation frequency, in the losses circuit. When the operation current is set as 3 A, the most easily oscillate mode is TE_{21} with the start length is 9.89 mm, and the corresponding oscillation frequency is 186.155 GHz, TE_{02} with start length 12.81mm at 394.84 GHz and TE_{11} with start length 15.94 mm at 166.78 GHz. It means that the nonlinear stage L_3 should be smaller than 9.89mm to avoid the backward wave oscillation. In Fig. 5 (b), the relationship between start length with conductance ($\sigma_{Cu} = 5.96e7$ S/m) is given. In order to ensure that the interaction gain is significantly large, the circuit length should be enough long. As the estimated whole length of the circuit is about 65 mm, and the corresponding conductance threshold is 106 S/m. To ensure oscillations do not occur, finally, the lossy dielectric conductance is set as 58 S/m.

As a quartic polynomial, the dispersion Eq. 1 has four roots. Which are related to four traveling waves, growing wave, decaying wave, forward constant amplitude wave, and backward constant amplitude wave. Usually, the imaginary part of the growing wave is defined as linear growth rate. And the corresponding linear gain is described as follows:

$$\text{Gain} = 20\log_{10}\left(e^{k_{zi}L}\right) \quad . \quad (4)$$

The changing trends of unity gain in the whole bandwidth, under the different lossy situations, are shown in Fig. 6. When the conductivity decreases, the loss increases, and the gain per unit length also decreases significantly. In addition, the operating bandwidth is extended to both high and low frequencies. As conductance is 58 S/m, the max value of linear gain is about 9 dB/cm. When the interaction circuit is 64 mm, the total gain is bigger than 55 dB, which also can be seen in Fig. 9.

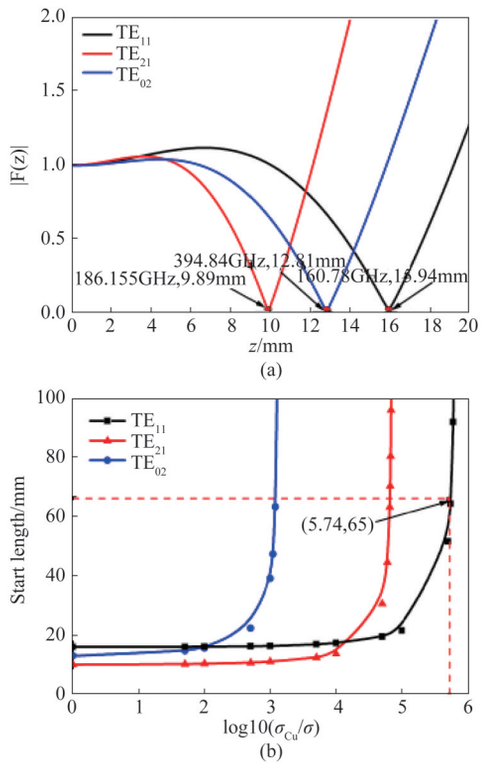

Fig. 5 The start length of backward wave oscillations with voltage $U_0 = 70$ kV and current $I = 3$ A, (a) longitudinal field profiles in losses circuit, (b) start length changing versus different conductance

图5 当电压为70 kV,电流为3 A时,返波振荡的起振长度(a)无损损耗波导中的纵向幅值曲线,(b)不同电导率情况下的起振长度

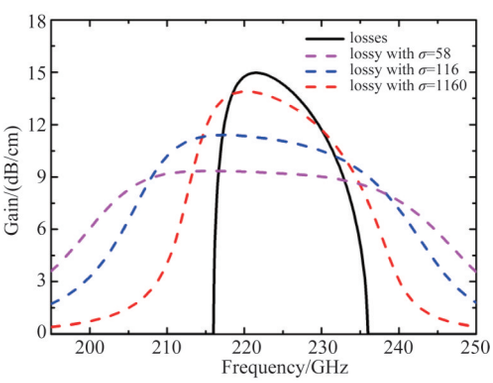

Fig. 6 The linear gain versus frequency with losses and different conductance lossy circuit ($U_0 = 70$ kV, $I = 3$ A, $\alpha = 1.2$, $b = 0.98$)

图6 线性增益在无损及不同电导率损耗电路情况下,随电压变化情况

1.3 Nonlinear theory analysis

In real operation situation, the high-frequency field cannot sustain the exponential growth as predicted in linear theory. Rather, it decreases after reaching a maximum value, this phenomenon is known as saturation. It is mainly caused by the over-bouncing of electron beam, also the nonlinear characteristic of the beam-wave interaction. Therefore, in order to study the interaction more deeply and accurately which includes the nonlinear changing trend of field amplitude and the variation of beam power, wave power, and lost power, nonlinear theory is necessary. The nonlinear used in this paper is electron kinetic theory [3-4], which is combined with six electron kinetic equations and a high frequency field equation.

Using nonlinear theory to calculate the axial field amplitude variation. And, the axial field amplitude can be divided into forward wave and backward wave. The normalized field profiles of three mainly backward wave oscillation modes are shown in Fig. 7. Start length of TE_{21}, TE_{11}, TE_{02} are calculated as 10.1 mm, 16.1 mm and 14.41 mm, respectively. Not only the start lengths, but the oscillation frequencies also are basically consistent with the linear theoretical calculation results. For restricting of backward wave oscillations, the nonlinear stage length L_3 is set as 9.5 mm.

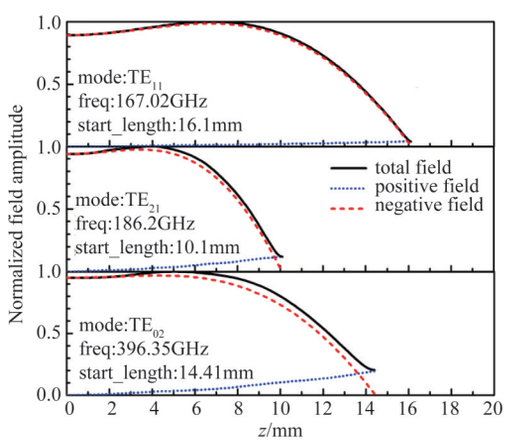

Fig. 7 The normalized field profiles of three backward wave oscillations in losses circuit (U_0 = 70 kV, I = 3 A, α = 1.2, b = 0.98)

图7 三个返波振荡模式在无损波导中的归一化幅值曲线 (U_0 = 70 kV, I = 3 A, α = 1.2, b = 0.98)

First, due to the length of the superconducting magnets uniform part in our laboratory is 65 mm. Therefore, the length of the overall interaction structure is set at about 65 mm. Secondly, in order to ensure that the input coupler has enough space for modulation and that the length of the smooth output section is less than the oscillation start length, the lengths of the smooth input end and the smooth output section are set to 4.5 mm and 9.5mm respectively. So, the initial length of the PDL section was set around 51 mm. Furthermore, as a single-mode theory, the influence of the competing mode is ignored, so the analysis of the PDL section structure mainly focuses on the number of periods and the dielectric slot ratio (L_d/L_p, L_d is media width, L_p is the cycle width). As shown in the Fig. 8 (a), the effect of the number of periods on the output power and gain, when L_d/L_p = 0.83. It can be seen, when the dielectric slot ratio is fixed, as the number of periods is 21, the output power reaches the maximum of 69.88 kW and the gain is 53.67 dB. When the number of periods decreases, the width of the dielectric in a single period increase, the working mode has more energy entering the dielectric area, which increases the loss of the signal and affects the modulation of the electrons. The clustering state is not enough to release a large amount of energy, resulting in a decrease in output power. When the number of periods increases, although the dielectric width becomes smaller, and the loss to the signal decreases, but it will cause the over-clustering of electrons, which will cause the interaction to enter the supersaturation state in advance, and the output power decreases. Figure 8 (b) shows the effect of the dielectric slot ratio on the output power and gain when the number of periods is 21. When the dielectric slot ratio is smaller, the dielectric width will be larger. Otherwise, the dielectric width will be smaller, and the loss of the working mode will change, which will affect the modulation state of the electrons, thereby affecting the output performance. In order to ensure the optimal performance of the Gyro-TWT, the total length of the dielectric rings loading section is finally set to 50.4 mm, of which the number of periods is 21, the period width L_p is 2.4mm, and the dielectric width L_d is 2 mm. The overall lenght of interaction structure is 64.4 mm.

The linear gain and nonlinear gain versus circuit length are shown in Fig. 9. We can see, at 220 GHz, the profiles of two gains in the linear stage keep pretty high consistency. The difference between the two gains is named launching loss and is caused by, in the input power, only the growing wave part contributes to the gain, and the decaying wave produces a negative gain in the beginning (L_0) and a part of input signal energy is used on the bouncing of electrons. In the nonlinear stage, as losses waveguide, the nonlinear gain increases significantly, and gradually approaches saturation.

Besides, the variation of beam power P_{beam}, wave power P_{out} and loss power P_{loss} are calculated using nonlinear theory. Figure 10 shows the nonlinear theory analysis results of P_{beam}, P_{out} and P_{loss} at 220 GHz, when U_0 = 70 kV, I_0 = 3 A, B = 8.16 T, alpha = 1.2, P_{in} = 0.3 W and σ = 58 S/m, the results satisfy the law of conservation of energy. The sum of lost power and wave power equals the loss of beam power. The P_{out} is amplified along the propagation direction and saturated at z = 64 mm. Where the output power is 69.88 kW, the efficiency is 33.28% and the gain is 53.67 dB.

As a single-mode theory, the nonlinear theory cannot calculate the multi modes of competition and also neglected the space charge influence. So, Using the electromagnetic simulation software, to do the PIC simulation

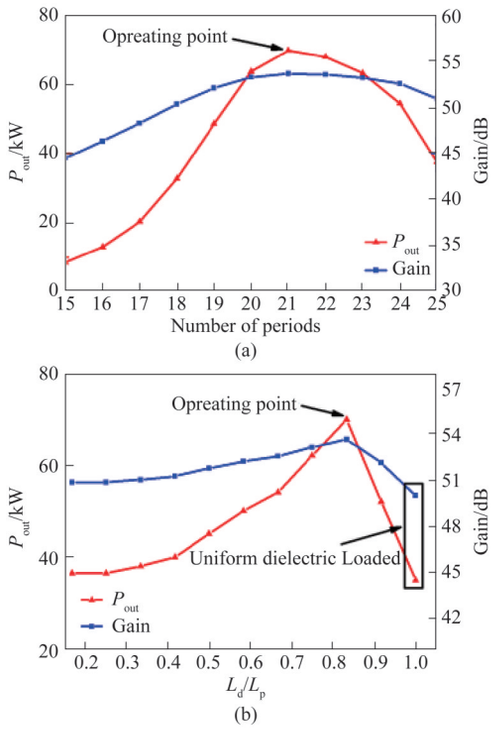

Fig. 8 At 220 GHz, U_0 = 70 kV, I_0 = 3 A, B = 8.16 T, alpha = 1.2, P_{in} = 0.3 W, σ = 58 S/m (a) the effect of the number of periods on the output power and gain, when L_d/L_p = 0.83, (b) the effect of the dielectric slot ratio on the output power and gain when the number of periods is 21

图 8 在 220 GHz, U_0 = 70 kV, I_0 = 3 A, B = 8.16 T, alpha = 1.2, P_{in} = 0.3 W, σ = 58 S/m 的情况下(a) 在 L_d/L_p = 0.83 的情况下，介质周期数量对于输出功率和增益的影响，(b) 在介质周期数量为 21 时，介质周期比对于输出功率和增益的影响

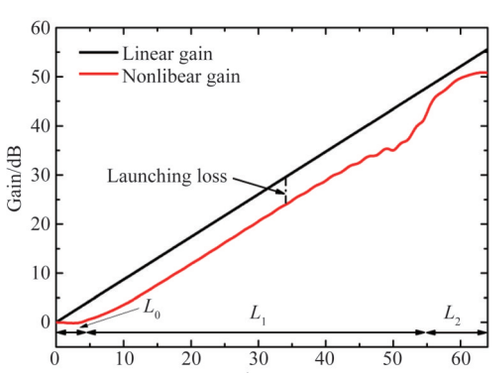

Fig. 9 At 220 GHz, comparison of gain versus interaction circuit length (U_0 = 70 kV, I_0 = 3 A, B = 8.16 T, alpha = 1.2, P_{in} = 0.55 W, and σ = 58 S/m)

图 9 在 220 GHz 时，线性增益与非线性增益曲线沿电路长度的变化。(U_0 = 70 kV, I_0 = 3 A, B = 8.16 T, alpha = 1.2, P_{in} = 0.55 W, and σ = 58S/m)

would get the more accurate results.

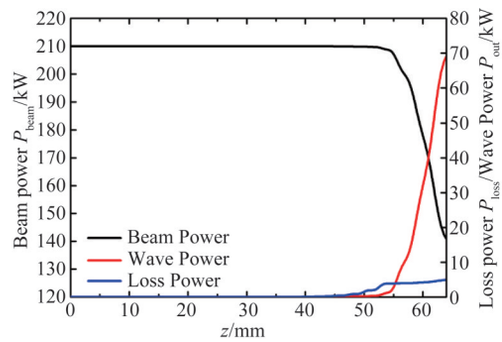

Fig. 10 P_{beam}, P_{out} and P_{loss} versus interaction circuit length (U_0 = 70 kV, I_0 = 3 A, B = 8.16 T, alpha = 1.2, P_{in} = 0.3 W and σ = 58 S/m, at 220 GHz)

图 10 在 220 GHz 时，电子注功率 P_{beam}，输出功率 P_{out} 和损耗功率 P_{loss} 沿电路长度的变化，(U_0 = 70 kV, I_0 = 3 A, B = 8.16 T, alpha = 1.2, P_{in} = 0.3 W, σ = 58 S/m)

2 PIC simulation

For further research of parasitic oscillations in this gyro-TWT, the backward wave oscillation of TE_{11}, TE_{02} also are observed and analyzed in 3D-PIC simulation (CST). Besides, the final optimized model has been proved zero drive stability and simulated in 3D-PIC simulation software. The detailed results of the PIC simulation are presented in the below sections.

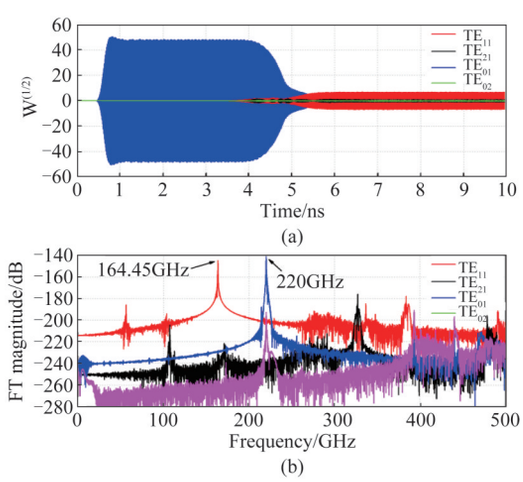

Fig. 11 The TE_{11} backward wave oscillation phenomenon (with TE_{01} as input signal at 220 GHz, U_0 = 70 kV, I_0 = 3 A P_{in} = 0.55 W L_0 = 4.5 mm, L_1 = 36 mm, L_2 = 9.5 mm, ε_r = 11 − 4.4 J, $r_o - r_w$ = 0.3 mm) (a) evolution of the quadratic root value of P_{peak} in the output part versus time (b) frequency spectrum of the output signals

图 11 TE_{11} 模式返波振荡现象(输入为 220 GHz 的 TE_{01} 模式，U_0 = 70 kV, I_0 = 3 A P_{in} = 0.55 W L_0 = 4.5 mm, L_1 = 36 mm, L_2 = 9.5 mm ε_r = 11 − 4.4 J $r_o - r_w$ = 0.3 mm)(a) 输出端口各模式的峰值输出功率平方根随时间变化曲线，(b) 输出端口各模式的频谱

2.1 Oscillation analyses in the PIC simulation

The TE_{11} backward wave oscillation phenomenon results are shown in Fig. 11, when $r_o - r_w = 0.3$ mm. Fig. 11(a) is the evolution of the peak power's (P_{peak}) quadratic root value of four modes, TE_{11}, TE_{21}, TE_{01}, TE_{02}. Meantime, the average power $P_{average}$ is half of P_{peak}. We can see that, at about 1ns to 4ns, the power of TE_{01} is stable out in the ouput port. And after 4 ns, the power of TE_{11} grows gradually, then the operational mode's power lost the dominated position, the TE_{11} backward wave oscillation is established. Figure 11 (b), the frequency spectrum, clearly shows that the frequency of backward wave oscillation mode TE_{11} is 164.45 GHz which is basically consistent with the theoretical study, although the working status is suppressed, the frequency spectrum of TE_{01} also can clearly see the operational frequency 220 GHz.

$$\varepsilon_r = \varepsilon_{re}\left(1 - \frac{j\sigma}{\omega\varepsilon_{re}}\right) \quad . \quad (5)$$

It needs to be mentioned here, as we have determined the dielectric conductance as 58 S/m, in the CST simulation, the conductance has been transformed into a complex relative dielectric constant by the Eq. 5.

As the nonlinear stage length is already smaller than the start length of TE_{11}. So, the attenuation of dielectric with $\varepsilon_r = 11 - 4.4$ J versus the dielectric thickness has been studied and is shown in Fig. 12. When dielectric thickness equals 0.3 mm, the attenuation of TE_{11} is pretty smaller. For successfully suppressing the TE_{11} backward wave oscillation, the thickness is set to 0.43mm where the attenuation of TE_{11} is maximum in around, and the attenuation of TE_{01} is as small as possible which will keep enough gain for the amplify.

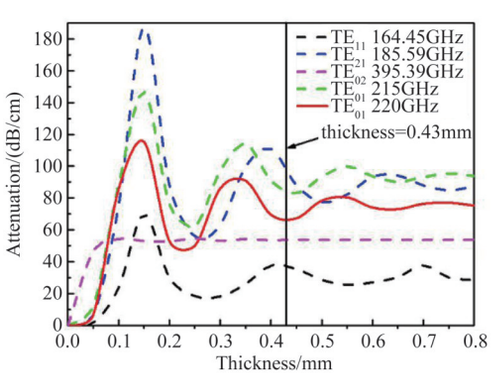

Fig. 12 Attenuation of dielectric versus the dielectric thickness with $\varepsilon_r = 11 - 4.4$ J

图12 当介质参数为$\varepsilon_r = 11 - 4.4$ J时,介质衰减与介质厚度的关系

In addition, the TE_{21} backward wave oscillation also has been observed, when $L_2 = 10.2$ mm, $r_o - r_w = 0.43$ mm, the results are shown in Fig. 13. At about 8.5 ns, TE_{21} gradually occupied the dominant position and TE_{01} output signal is affected and decreases significantly. The frequency spectrum also shows that the oscillation frequency of TE_{21} is 185.59 GHz. And in the optimized process, when L_2 smaller than 9.8*mm*, this oscillation is disappeared. Thus, the oscillation of TE_{21} also proved the correctness of theoretical studies. In the process of the optimized simulation, TE_{02} backward wave oscillation and TE_{01} absolute instability oscillation are not caught.

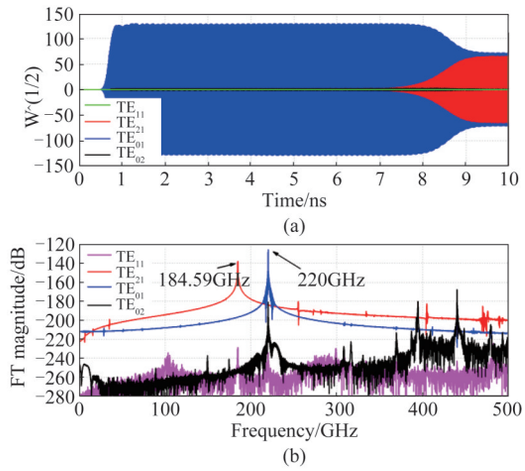

Fig. 13 The TE_{21} backward wave oscillation phenomenon (with TE_{01} as input signal at 220 GHz, $U_0 = 70$ kV, $I_0 = 3$ A $P_{in} = 0.55$ W $L_0 = 4.5$ mm, $L_1 = 36$ mm, $L_2 = 10.2$ mm $\varepsilon_r = 11 - 4.4$ J $r_o - r_w = 0.43$ mm) (a) evolution of the quadratic root value of P_{peak} in the output part versus time, (b) frequency spectrum of the output signals

图13 TE_{21}模式返波振荡现象(输入为220 GHz的TE_{01}模式,$U_0 = 70$ kV, $I_0 = 3$ A $P_{in} = 0.55$ W $L_0 = 4.5$ mm, $L_1 = 36$ mm, $L_2 = 10.2$ mm $\varepsilon_r = 11 - 4.4$ J $r_o - r_w = 0.3$ mm) (a) 输出端口各模式的峰值输出功率平方根随时间变化曲线,(b) 输出端口各模式的频谱

Table 1 Design parameters of 220 GHz Gyro-TWT

表1 220 GHz回旋行波管的设计参数

Parameters	Specifications
Beam voltage U_0	70 kV
Beam current I_0	3 A
Velocity pitch factor α	1.2
Waveguide radius r_w	0.85 mm
Dielectric thickness ($r_o - r_w$)	0.43 mm
Guiding center radius r_g	0.46*r_w
Operating mode	TE_{01}
Dielectric property (Beo-Sic)	11~4.4 J
Operating magnetic field B_0	8.16 T
Structure length L_0, L_1, L_2	4.5 mm, 50.4 mm, 9.5 mm
Dielectric slot ratioL_d/L_p	0.83
Period lengthL_p	2.4 mm

2.2 Optimized PIC simulation results

After a series of optimization, the final design parameters of gyro-TWT have been determined and are

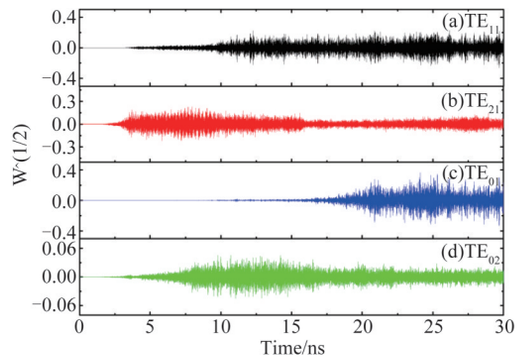

Fig. 14 Output port signal of the four mainly competitional modes versus the simulation time at zero drive

图 14 四个主要竞争模式在零驱动情况下的输出信号幅值随时间变化情况

listed in Table 1.

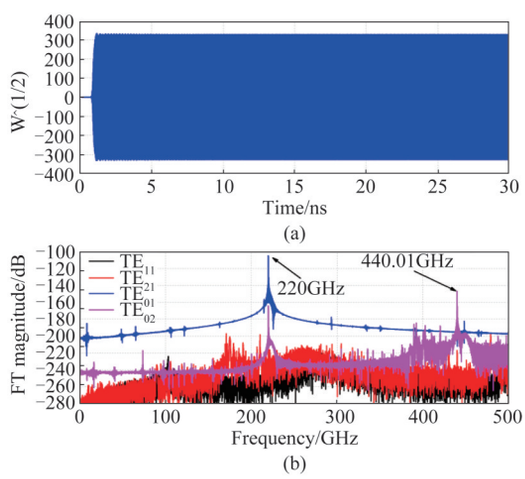

Fig. 15 The 3D-PIC simulation results of optimized model (P_{in} = 0.55 W, at 220 GHz) (a) evolution of the quadratic root value of P_{peak} in the output port versus time, (b) frequency spectrum of the output signals

图 15 优化后的 3 维粒子仿真结果 (P_{in} = 0.55 W, 输入信号频率为 220 GHz) (a) 输出端口各模式的峰值输出功率平方根随时间变化曲线,(b) 输出端口各模式的频谱

Figure 14 demonstrates the evolution of four competition modes signal at the output port in zero drive situation. The output signals of modes show the significant characters including ignorable growth and a relative low level, which means that all parasitic oscillations have been suppressed completely.

Figure 15 (a) is the output signal of the operating mode TE_{01} in the output port. And Fig. 15 (b) is the frequency spectrums of TE_{01} and three main competition modes. After the post processing of CST, the simulation predicted average power of about 55.61 kW at 220 GHz. From Fig. 15 (b), we also can see that, the competition modes are suppressed pretty well, no clear oscillation frequency occurred, and only the second harmonic frequency 440.01 GHz is caught in the TE_{02} spectrum which is no impact on the stable operation.

2.3 Comparison of simulation results

In this part, the nonlinear theory simulation results, 3D-PIC simulation results are compared. Figure 16 is the comparison of output power versus frequency between nonlinear numerical program and 3D-PIC simulation. It's clearly that the 3D-PIC simulation output power reaches 55.61 kW at 220 GHz. Meantime the output power under two simulation ways basically keeps the same trend and is greater than 45 kW between 219 GHz and 226 GHz. The -3 dB bandwidth is 217.5 GHz to 229.5 GHz, about 12 GHz. The comparison of output power gain versus different input power also is analyzed and shown in Fig. 17. In this figure, the overall trend of gain curves basically agrees with each other. In the area where the input power is smaller than 0.1 W, the gain is almost saturated and the saturated gain of CST simulation is 53.56 dB. When input power equals 0.55 W, the gain is about 49.46 dB. As the input power increases, when it is greater than 1 W, the gain decreases rapidly.

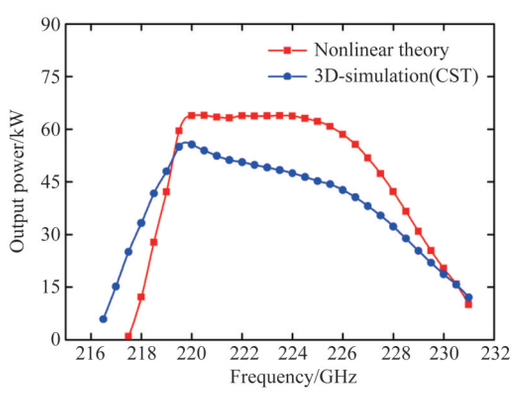

Fig. 16 Comparison of output power versus frequency with P_{in} = 0.55 W at 220 GHz

图 16 输出功率随频率的变化曲线对比,(输入信号为 220 GHz,输入功率为 0.55 W)

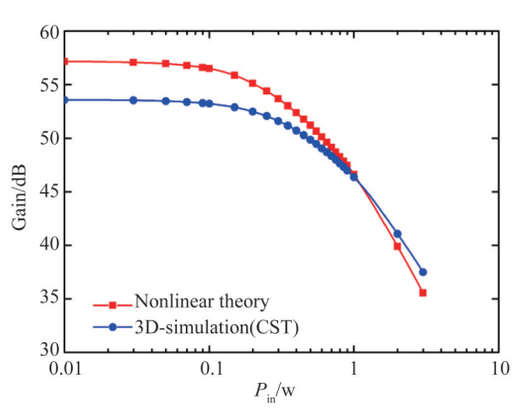

Fig. 17 Comparison of output power gain versus P_{in} at 220 GHz

图 17 输出增益随输入功率的变化曲线对比,(输入信号为 220 GHz)

3 Conclusions

The fundamental harmonic 220 GHz PDL gyro-TWT operating at TE_{01} has been designed, by theoretical absolute instability oscillation and backward wave oscillations are predicted by theoretical studies, verified by the CST 3D-PIC simulation, and suppressed successfully. The CST 3D-PIC simulation results show that the saturated output power reaches 55.61 kW at 220 GHz with gain of 49.46 dB, and the efficiency is 26.48% with the beam voltage of 70 kV, beam current of 3 A, and the velocity pitch factor of 1.2. The saturated gain is 53.56 dB, and the -3 dB bandwidth is 12 GHz. The performance of gyro-TWT is compared by the nonlinear numerical program, CST 3D-PIC simulation, whose results are basically consistent.

References

[1] Thumm M. State-of-the-art of high-power gyro-devices and free electron masers[J]. *Journal of Infrared, Millimeter, and Terahertz Waves*, 2020, **41**(1):1-140.

[2] Chu K R. Overview of research on the gyrotron traveling-wave amplifier[J]. *IEEE Transactions on Plasma Science*, 2002, **30**(3):903-908.

[3] Du C H, Liu P K. Millimeter-wave gyrotron traveling-wave tube amplifiers[M]. Springer Berlin Heidelberg, 2014.

[4] Chu K R, Chen H Y, Hung C L, *et al*. Theory and experiment of ultrahigh-gain gyrotron traveling wave amplifier[J]. *IEEE Transactions on Plasma Science*, 1999, **27**(2):391-404.

[5] Yan R, Tang Y, Luo Y. Design and experimental study of a high-gain W-band gyro-TWT with nonuniform periodic dielectric loaded waveguide[J]. *IEEE Transactions on Electron Devices*, 2014, **61**(7):2564-2569.

[6] Sirigiri J R, Shapiro M A, Temkin R J. High-power 140-GHz quasi-optical gyrotron traveling-wave amplifier[J]. *Physical review letters*, 2003, **90**(25):258302.

[7] Nanni E A, Jawla S, Lewis S M, *et al*. Photonic-band-gap gyrotron amplifier with picosecond pulses[J]. *Applied Physics Letters*, 2017, **111**(23):233504.

[8] Liu D, Tang X, Yan Y, *et al*. Design of confocal waveguide interaction structure for a 220 GHz gyro-TWT[J]. *Journal of ElEctromagnEtic WavEs and applications*, 2017, **31**(6):650-662.

[9] An C, Zhang D, Zhang J, *et al*. Theoretical analysis and PIC simulation of a 220-GHz second-harmonic confocal waveguide gyro-TWT amplifier[J]. *IEEE Transactions on Electron Devices*, 2019, **66**(9):4016-4021.

[10] Wang E, Zeng X, Liu B, *et al*. Experimental study of high-power gyrotron traveling-wave tube with periodic lossy material loading[J]. *IEEE Transactions on Plasma Science*, 2012, **40**(7):1846-1853.

[11] Du C H, Chang T H, Liu P K, *et al*. Design of a W-band gyro-TWT amplifier with a lossy ceramic-loaded circuit[J]. *IEEE transactions on electron devices*, 2013, **60**(7):2388-2394.

[12] Thottappan M. Design and efficiency enhancement studies of periodically dielectric loaded W-band gyro-TWT amplifier[J]. *IEEE Transactions on Electron Devices*, 2020, **67**(7):2925-2932.